# Integration of an isotropic microprobe and a microenvironment into a conventional CMM

OPEN ACCESS
IOP Publishing
Measurement Science and Technology
Meas. Sci. Technol. **30** (2019) 115007 (15pp)
https://doi.org/10.1088/1361-6501/ab2fda

# Integration of an isotropic microprobe and a microenvironment into a conventional CMM

**D Metz[1,4], S Jantzen[2,4], D Wessel[2], G Mies[3], J Lüdenbach[3], M Stein[2], K Kniel[2] and A Dietzel[1]**

[1] Technische Universität Braunschweig, Institute of Microtechnology (IMT), Alte Salzdahlumer Str. 203, 38124 Braunschweig, Germany
[2] Department of Coordinate Metrology, Physikalisch-Technische Bundesanstalt (PTB), Bundesallee 100, 38116 Braunschweig, Germany
[3] Klingelnberg GmbH, Peterstraße 45, 42499 Hückeswagen, Germany

E-mail: d.metz@tu-bs.de

Received 11 April 2019, revised 21 June 2019
Accepted for publication 4 July 2019
Published 4 September 2019

**Abstract**

This paper describes the experimental verification of the novel IMT-PTB microprobe combined with a uniquely designed microenvironment. The microprobe consists of three silicon-based parallelograms stacked orthogonally, which leads to high isotropy. The probe tip deflections are detected in 3D with the help of piezoresistors placed in the parallelograms. The microenvironment facilitates and improves the measurement of workpieces with sub-millimeter features. The new microprobe and the microenvironment were integrated into a commercial coordinate measuring machine (CMM). To evaluate the microprobe performance, PTB produced and calibrated three reference objects: a cube, a sphere, and a microgear measurement standard. The differences between the calibration values and the measurement results obtained by the microprobe were in the sub-micrometer range. Furthermore, the microprobe was compared with the standard probing system of the gear measuring machine by measuring the reference objects with identical parameters. The results show the excellent performance of the micro probing system, thereby extending the capability of the CMM for high-precision measurements of complex workpieces at the microscale.

Keywords: tactile measurement, coordinate metrology, silicon isotropic microprobe, microgear measurement standard, microenvironment, gear measuring machine

(Some figures may appear in colour only in the online journal)

## 1. Introduction

Workpieces with sub-millimeter features are vital components in many industrial products. A large share of their quality control relies on dimensional measurements with small measurement uncertainties. To meet the requirements, measuring 3D features at the microscale with high precision demands special tools. Tactile probing techniques enable highly accurate measurements of geometries with small measurement uncertainty and are, next to the optical methods, the most used method. Probing systems are mostly composed of a measuring system, which senses the position of the probing element (e.g. a probing ball on a stylus) brought into contact with the workpiece during the measurement [1] by considering the 3D deflection of the stylus. In a coordinate measuring machine (CMM), the geometries of the workpiece are determined by sampling and evaluating measurement points according to the respective geometry parameters.

Several tactile microprobes have been developed in the past [2], and some have been commercialized for the use in special $\mu$CMM [3–9]. These microprobes consist of highly sensitive sensors based on different physical principles to assure

[4] Both authors contributed equally to this work.

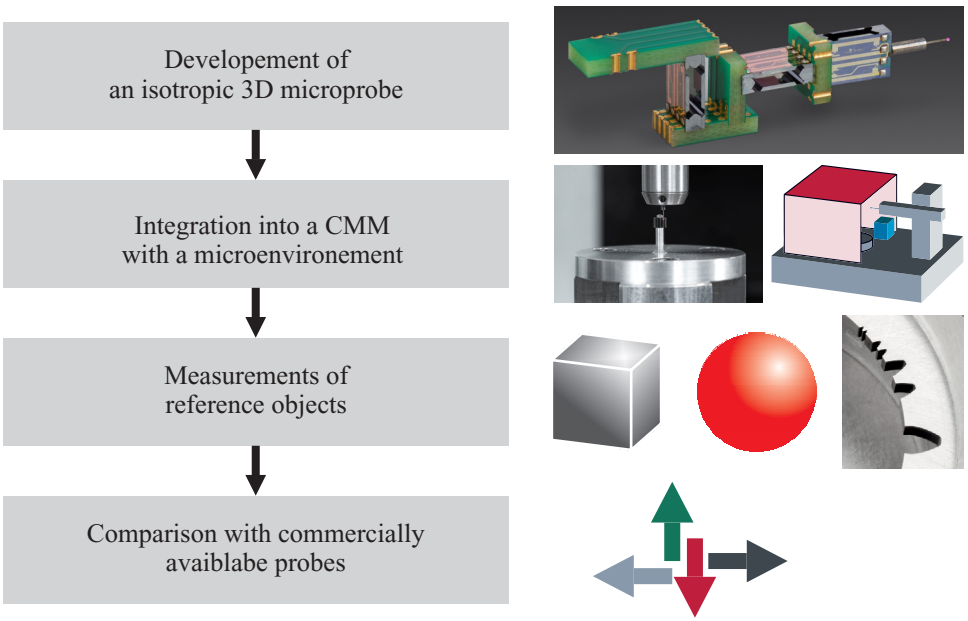


**Figure 1.** Methodology and content of this paper.

sub-micrometer resolution using optical [10, 11], capacitive [12], inductive [13] or piezoresistive principles [14–17]. Their mechanical structure or probing element suspension with little stiffness allow low probing forces. *Non-contact* probing can also be achieved by vibration detection principles [6, 18, 19] to avoid the potential deterioration of the probed surfaces by reducing contact forces.

Microprobes made from monocrystalline silicon [14–17] exhibit excellent mechanical properties. Due to the linear-elastic and temperature-independent [20–22] mechanical behavior as well as the excellent fatigue resistance [23], silicon is the *perfect* material for flexible structures at the microscale. The *strong piezoresistive effect* of silicon (about 50–100 times higher than for metals) [24, 25] allows a high integration level of extremely sensitive sensors in thin mechanical constructions. Besides the integration benefits, silicon permits the use of advanced fabrication processes at wafer level offering low cost and high manufacturing accuracy and reproducibility. Nevertheless, silicon microprobes usually show small deflection ranges, 100 μm or even less than 50 μm depending on the probing direction and a *strong anisotropy* resulting from the membrane-based designs (e.g. silicon membrane). High anisotropies decrease the measurement quality for inclined surfaces because of the slipping of the probe tip. Silicon isotropic mechanical designs have been developed with the drawback of increased stiffness and further decreased maximum probe deflection, which is disadvantageous for industrial use [26–28].

Measurements at the microscale are challenging [29–32]: manual handling of the small objects may be difficult; the human eyesight is limited; contamination can easily impair tactile measurement results; objects at the microscale are often fragile. To assists the user during measurement setup, to protect and monitor the environment, and to feature cleaning and clamping systems, the developed microenvironment and tools are also here reviewed.

Because of the challenges for measurements at the microscale, the measurement of micro-geometries is still reserved for specific, high-accuracy, and expensive $\mu$CMM, limiting their access to a few companies and institutes. Typical measurements of micro-geometries on small workpieces (>1 cm) are not possible or exceedingly difficult on conventional CMMs because of the need and use of small probing elements (<Ø 300 μm) and usually not because of a lack of handling support for such small workpieces.

In this work, a complete micro coordinate metrology solution for a conventional CMM is proposed; integration of a new IMT-PTB microprobe (developed in collaboration of the Institute of Microtechnology with Physikalisch-Technische Bundesanstalt) and a microenvironment, both allowing and facilitating micromeasurements on the Klingelnberg P40. To verify this solution, measurements were performed on calibrated reference objects and compared. Previous works on a silicon membrane-based microprobe have demonstrated the advantages and limitations of integrating such microprobes into CMMs [14, 33–35]. With the goal to facilitate this integration, a novel silicon microprobe based on a parallelogram design has been developed, presented [36, 37] and patented [38]. The proposed construction composed of three silicon parallelograms stacked orthogonally provides isotropic kinematics with large measuring ranges, little stiffness, and high sensitivity due to piezoresistors in doped monocrystalline silicon used as sensors. This novel IMT-PTB microprobe, contained in a Ø 11 mm housing, is a first silicon-based miniaturization of the probing system based on a three parallelogram construction proposed by Zeiss in 1973 [1] or of the microprobe proposed by METAS [3, 13].

The microenvironment developed in conjunction with the IMT-PTB microprobe aims at overcoming the practical challenges for dimensional measurements at the microscale such as clamping of microworkpieces and technical cleanliness. Therefore, the microenvironment comprises four systems: passive separative device, microgear clamp, dual-camera system, an online sensor system (live tracking temperature, humidity, and particle density), and a $CO_2$ snow cleaning system.

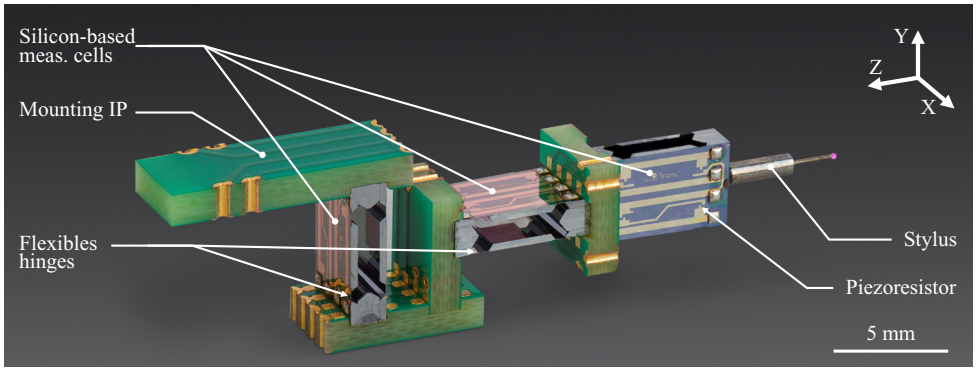


**Figure 2.** The microprobe developed at IMT featuring three stacked parallelograms.

In the first section of this paper, an overview of the novel IMT-PTB microprobe, its working principle, and its properties will be given. Then, its integration in the P40 and its characterization will be detailed and validated towards the standard probing system. Finally, to evaluate the microprobe performances, PTB produced and calibrated three reference objects: a cube, a sphere, and a microgear measurement standard. Results of the artifact measurements with the microprobe were evaluated and compared to those with the standard probing system, and to the calibration values (see figure 1).

## 2. 3D tactile microprobe

The novel silicon-based microprobe provides many advantages towards other commercial silicon-based probe designs. Both, a large measuring range and an isotropic behavior can be achieved without compromises on one of each or the overall system size. This novel design facilitates integration and use in conventional CMMs for tactile measurements. Its operating principle, fabrication process, and properties are summarized below (see [36–38] for more details). The microprobe and its single sensing elements have also been used as force sensors for the mechanical characterization of micromechanical systems (e.g. microgrippers) and skeletal muscle tissue [39, 40].

### 2.1. Working principle

The IMT-PTB microprobe used in this work consists of three orthogonally stacked silicon-based measurement cells. The parallelogram structure of the measurement cells, built by elastic hinges made of thin silicon membranes, allows a deflection of the cell in only one direction over a wide range. This deflection is detected and measured utilizing the strong piezoresistive effect of doped silicon. The working principle of the measurement cell is similar to those of conventional bending force transducers or load cells, by which strain sensors are placed on the structure, to measure the applied deflection and force [41–43]. The orthogonal stacking of three identical measuring cells provides an isotropic electromechanical suspension, which allows detecting the displacement of an attached probing element (e.g. a ruby ball mounted on a pin) in the three orthogonal axes $X$, $Y$ and $Z$, one per cell (see figure 2).

To detect the deflection of the measuring cells with high sensitivity, piezoresistors are embodied in the membranes, where the induced mechanical stresses are concentrated. In total, four piezoresistors wired in a full Wheatstone-bridge linearly transduce the membrane's deformation (the cell deflection) into a voltage. Out of the three voltages $U_X$, $U_Y$ and $U_Z$ of each measuring cell, the deflection of the probing elements $m_X$, $m_Y$ and $m_Z$ can be deduced by using a $3 \times 3$ conversion matrix $\boldsymbol{C}$, which is determined during the characterization of the microprobe. Ideally, $\boldsymbol{C}$ is a diagonal matrix, when the cells are perfectly orthogonal to each other and parallel to the axes of the measuring instruments, and if there is no crosstalk between the measuring cells. To compensate not perfectly ideal conditions, small non-diagonal coefficients can be introduced:

$$\boldsymbol{m} = \boldsymbol{C} \cdot \boldsymbol{U} \tag{1}$$

$$\text{with } \boldsymbol{m} = \begin{pmatrix} m_X \\ m_Y \\ m_Z \end{pmatrix} \text{ in mm; } \boldsymbol{U} = \begin{pmatrix} U_X \\ U_Y \\ U_Z \end{pmatrix} \text{ in V;}$$

$$\boldsymbol{C} = \begin{bmatrix} c_{xx} & c_{yx} & c_{zx} \\ c_{xy} & c_{yy} & c_{zy} \\ c_{xz} & c_{yz} & c_{zz} \end{bmatrix} \text{ in mm} \cdot \text{V}^{-1}.$$

### 2.2. Fabrication of the microprobe

The central components of the microprobe are the silicon-based measuring cells, which were built of two different silicon wall wafers (front and back) containing the silicon membranes (flexure hinges), the piezoresistors and the electrical wiring, and a third silicon spacer wafer (see figure 3(a)). The three wafers were microfabricated using standard photolithographic processes and bonded together at wafer level using a transfer adhesive bonding technique. Finally, a wafer saw separates the individual measuring cells. The processes to fabricate earlier membrane-based microprobe designs (see [14, 28]) were customized and optimized for the front and rear wall wafers. For the front wafer, a double-sided polished, n-doped {1 0 0} silicon wafer with a thickness of 360 µm ± 25 µm was used. Using a $p$- and a $p+$ doping with boron atoms (900 °C and resp. 1100 °C for 30 min), the piezoresistors were diffused in the silicon. After passivation of the upper side, the resistors

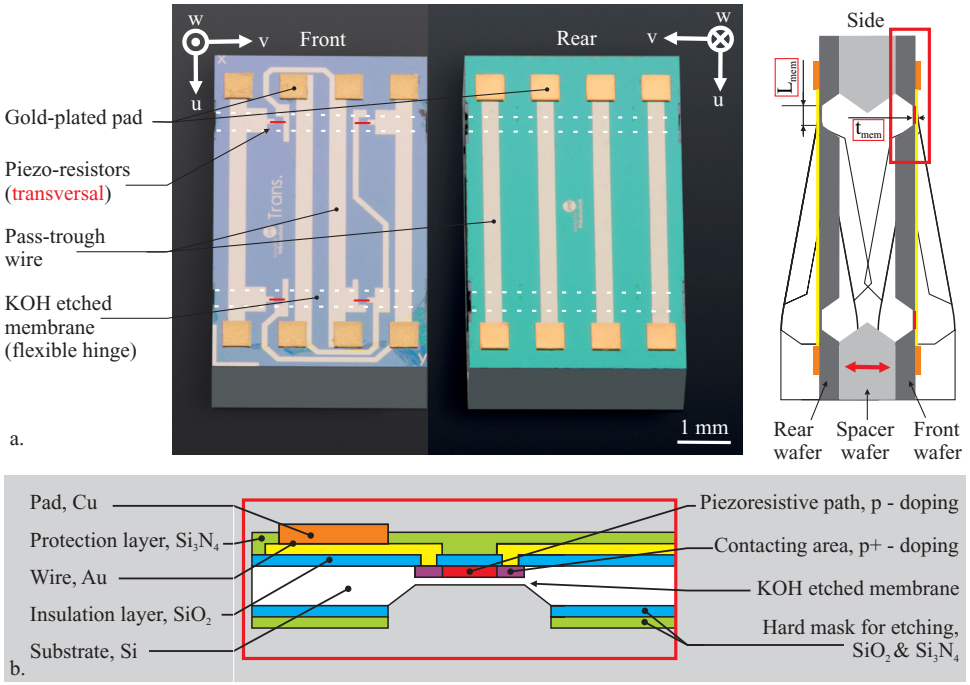


**Figure 3.** (a) Front, rear and side view of the silicon-based measurement cell and (b) schematic cross-section of the wafer-level fabricated front wafer with detail on the silicon membrane (flexure hinges) with the integrated piezoresistors and wiring.

were interconnected using gold traces. Additional gold-plated copper pads offer an excellent possibility for further contacting by soldering. The silicon membranes were etched over time in a 40% potassium hydroxide (KOH) solution at 80 °C using a silicon oxide and nitride hard mask (see figure 3(b)). The rear wafer is like the front wafer but contains only pass-through traces crossing the cell without piezoresistors (see figure 3(a)). The spacer wafers, which are made of a 1000 µm thick double-side polished, {1 0 0} silicon wafers, are free of electrical elements and were only wet-etched in KOH.

To build the microprobe, three measuring cells were mounted together with interposers (IP) to solve the challenge of their orthogonal stacking and contacting, and to provide a compact and robust system (see figure 2). The mounting IP allows clamping the microprobe in a holder and connecting it to the external power supply and evaluation electronics. A $2 \times 4$ pad array on the internal side of the mounting IP (side not visible in figure 2) can be securely wired with a contact spring array such as in the developed holder (see section 3.2). A common supply voltage was used for all three measuring cells to reduce the wiring effort in the microprobe. The voltage was transmitted to each cell using pass-through tracks on the IPs and those on the front of the cells. The voltages $U_X$, $U_Y$ and $U_Z$ are transmitted to the pad array using the tracks present on the rear of the cells. The custom-made IPs were manufactured by an industrial supplier as 1.6 mm thick printed circuit board (PCB) in FR4, a glass-reinforced epoxy laminate material. These were processed and then cut with a wafer saw (DAD320 from co. Disco). Industrial PCBs allow a low-cost and fast production with high-quality vias. IPs made of silicon, glass, or ceramics are conceivable but have not yet been investigated. Finally, the cells and IPs were glued together in an aluminum machined special tool presented in [37]. To ensure a perfect orthogonality, the cells were held against the tool's reference surfaces with vacuum when curing the adhesive (353ND, Co. Epotek, curing 5 min @ 150 °C). To complete the assembly, all tracks of the cells were hand-soldered to one of the IPs [37]. Finally, the stylus was glued on the microprobe. Automating the assembly for larger quantities is also possible and is currently under investigation. All experiments presented here took place in a climate-controlled laboratory (see section 4.2), needed for measurement with sub-micrometer accuracy, so that the thermal effect on the microprobe's glued and soldered construction made from silicon and FR4 could be neglected. In future work, temperature effects should be investigated for a typical industrial range (10 °C–40 °C).

### 2.3. Properties of the microprobe

The silicon-based measurement cell was designed to deflect only in its sensitive $w$-direction (see figure 3) over a broad range and with small stiffness. A complete and detailed characterization of the cell and the microprobe can be found in [37]. In the deflecting $w$-direction, stiffness $S_w$ in a range between $0.3\,\mathrm{N \cdot mm^{-1}}$ and $0.5\,\mathrm{N \cdot mm^{-1}}$ could be fabricated by using different hinge thicknesses $t_{\mathrm{mem}}$ and lengths $L_{\mathrm{mem}}$ (see figures 3 and 4). Probing forces smaller than 100 mN are possible even at 200 µm deflections. FEM simulated values of $S_w$ agree within the measured tolerance and can be used to predict mechanical properties (see figure 4). Special attention has to be paid to the fabrication of the membrane thickness $t_{\mathrm{mem}}$ as $S_w \propto t_{\mathrm{mem}}^3$ [37]. The facture deflection of similar measuring cells of up to 548 µm ± 64 µm has been observed enabling measurement ranges up to ±400 µm [36, 37]. Ideally, in the $u$- and $v$-directions, the cell is stiff and transmits forces to the

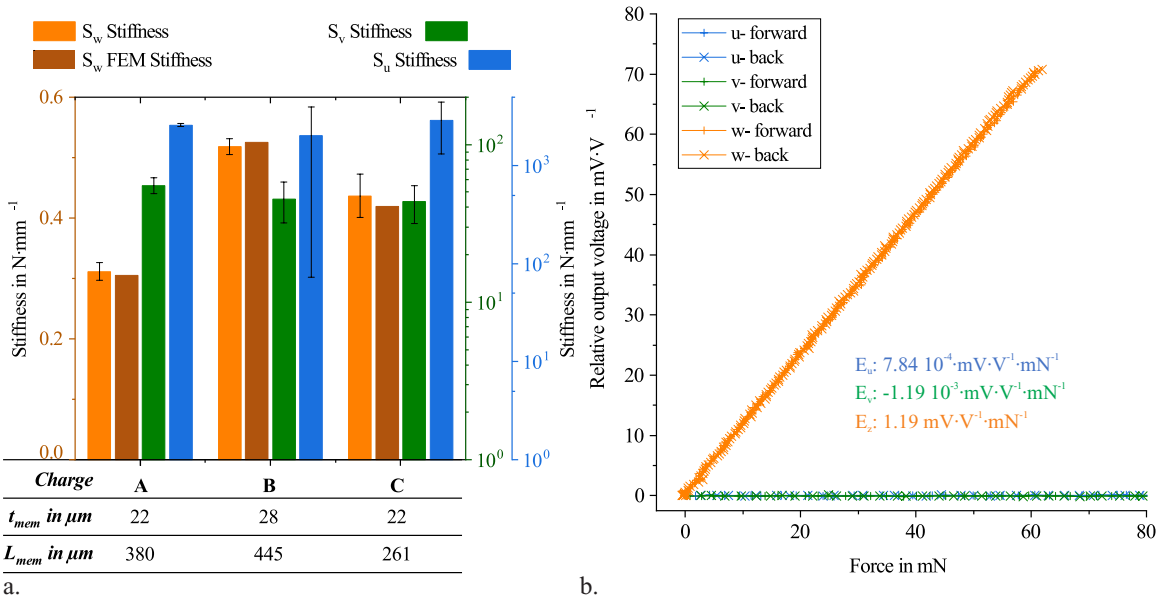


**Figure 4.** (a) Mechanical and (b) sensor characterization of typical SP in all directions for different SP charges with different hinge thicknesses $t_{\mathrm{mem}}$ and lengths $L_{\mathrm{mem}}$.

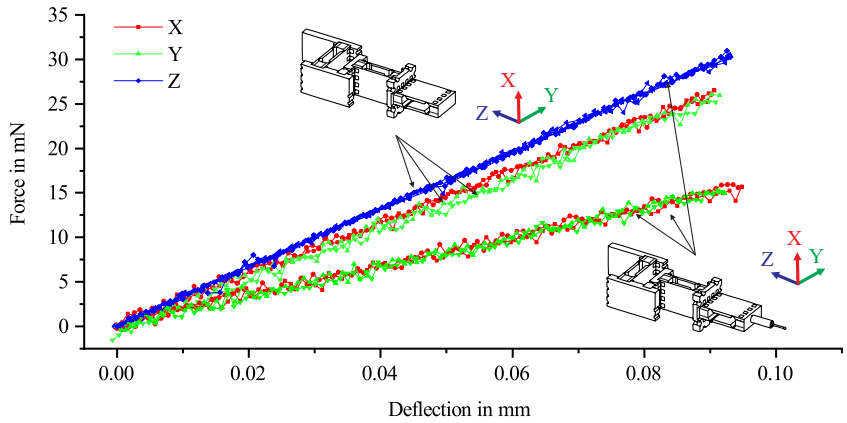


**Figure 5.** Force-over-deflection diagram of a microprobe for a 100 µm deflection range in $X$-, $Y$-, and $Z$-direction: without stylus and with stylus (0.1 mm probe diameter) [37].

next cell. In practice, infinite stiffness cannot be achieved, but a ratio between 90:1 and 300:1 of the stiffness $S_u$ or $S_v$ and $S_w$ can be achieved if one accepts the outer dimensions of fabricated parallelograms as given (figure 4). During probing, the microprobe is subjected to forces in the three directions $X$, $Y$ and $Z$, which leads to different forces on the measuring cell $i$ in the $u_i, v_i, w_i$-directions. The cells have to be sensitive only in their $w_i$-direction to eliminate crosstalk between the probing directions $X$, $Y$ and $Z$. Ratios between the sensitivities $E_u$ or $E_v$ and $E_w$ from 600:1 to 1500:1 could be obtained depending on the geometry of the three different fabricated cells. In figure 4, the sensitivity of the measurement cell related to the force applied in all $u, v, w$-directions are displayed for one cell geometry inexample.

The microprobe, like the cell itself, has an outstanding linear elastic behavior (force-to-deflection relation) with a relative linearity error $d_{\mathrm{lin}}$ lower than 0.94%. Additionally, an excellent linearity of the output voltage related to the deflection with a $d_{\mathrm{lin}} < 0.27\%$ was reported in [37] for a range of ±200 µm on $X$, $Y$, and +200 µm on $Z$. Crosstalk could be reduced to 2%–4% between all axes by improving the fabrication and assembly.

Due to the use of identical cells, isotropic electrical and mechanical behavior can be achieved. Without a stylus, the system is perfectly isotropic whereas a small anisotropy appears with a stylus. The bending of the stylus in its radial directions ($X$-, $Y$-directions) leads to a mechanical anisotropy up to 2:1, which is lower than every silicon membrane based on microprobes with low stiffnesses ($<0.4\,\mathrm{N}\cdot\mathrm{mm}^{-1}$). Furthermore, by re-adjusting the measuring cell geometry depending on their position in the microprobe, the mechanical anisotropy could be eliminated (for example, by adjusting the membrane thicknesses). To test the properties of the microprobe in a harsh condition, mechanical and electrical characterization have been carried out with an electro-discharge machined stylus [44] with a 0.1 mm probing sphere diameter, a 2 mm tapered shaft and a total length of 10 mm. Figure 5 and figure 6(a) show the mechanical behavior of the microprobe with and without the stylus and confirms the influence on the microprobe of the latter, by increasing the mechanical anisotropy up to 1.4:1. In

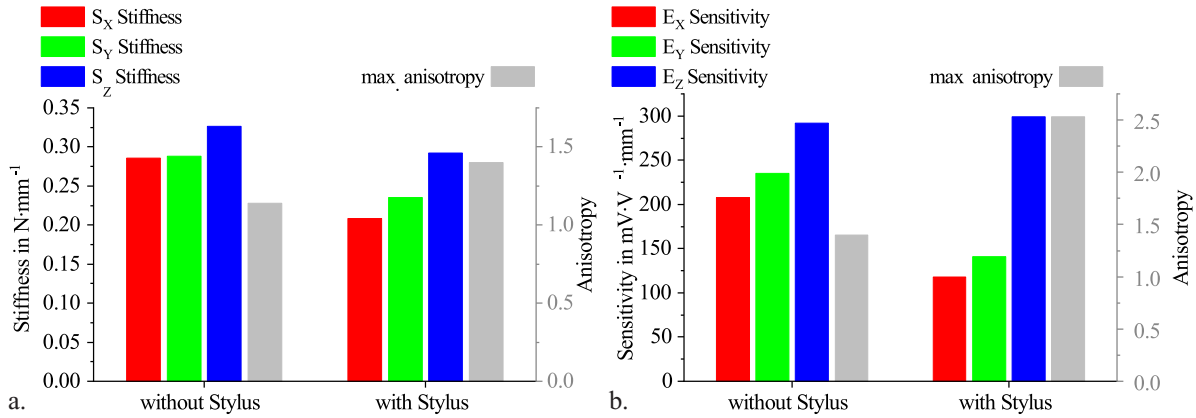


**Figure 6.** (a) Measured stiffnesses and (b) sensitivities in $X$-, $Y$-, and $Z$-direction for a microprobe with and without stylus for a $\pm 200\,\mu m$ measurement range [37].

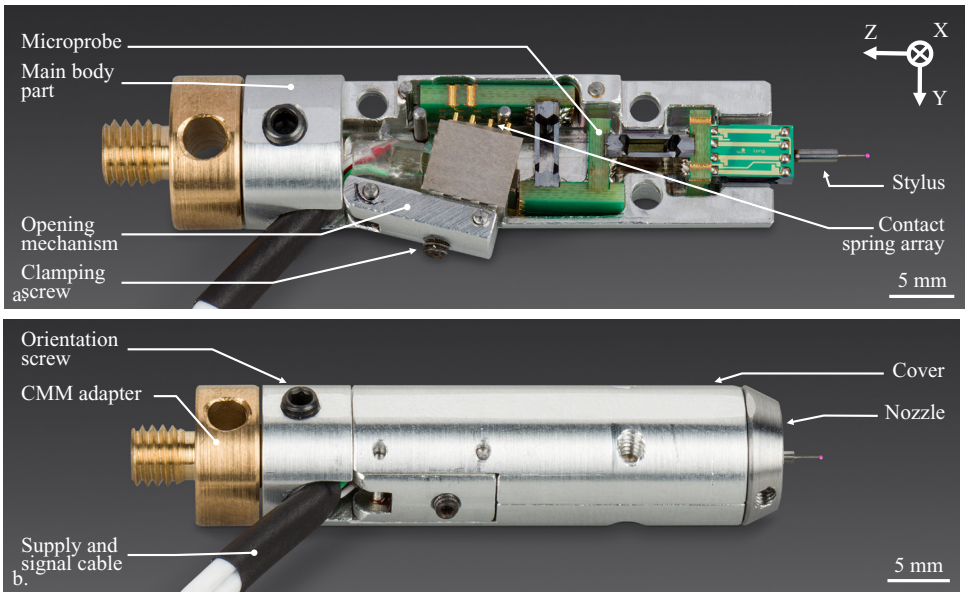


**Figure 7.** (a) Opened, and (b) closed housing for a 3D microprobe.

figure 6(b), the determined stiffnesses and sensitivities with the corresponding anisotropy are displayed. The sensing anisotropy of about 2.5:1 can be compensated during the calibration of the sensor in the CMM (see section 3.3). The current resolution is approximately 200 nm to 500 nm and is currently investigated to reach a competitive level such as 10 nm.

The measurements presented in section 4.3 were carried out with a microprobe featuring a commercial stylus with a ruby probing sphere, which is presented in figure 2. Its mechanical anisotropy of 1.1:1 and its stiffnesses in $XY$-direction of approx. $0.32\,N \cdot mm^{-1}$ were determined. The stylus has a probe tip diameter of 300 µm, a 2 mm shaft and a total length of 5 mm.

## 3. Integration of the microprobe and of a microenvironment into a gear measuring machine

### 3.1. Description of the CMM

The microprobe was integrated into the P40 CMM of Klingelnberg GmbH. The probing head (in the following named: M44) can be moved along three linear axes $(X, Y, Z)$ and has a coupling system with which various styli mounted on a changing plate can be automatically exchanged. The workpiece placed on a rotary table can be rotated on the $C$ axis (in $Z$-direction), which makes this machine particularly suitable for axially symmetrical parts (e.g. gears). For tactile measurements, the induced deflections $M_X, M_Y, M_Z$ and the position relative to the workpieces $P_X, P_Y, P_Z, P_C$ of the M44 are used to determine the geometry of the workpiece or its deviations from a nominal geometry. More details about the CMM can be found in [45, 46].

### 3.2. Mechanical and electrical interface of the microprobe

For the microprobe, a housing was developed to hold, contact, and protect the microprobe during its use and handling in the measuring machine (see figure 7). The microprobe is inserted into the housing composed of an aluminum body and clamped by a screw. The microprobe signals are contacted with a $2 \times 4$ spring contact array wired to external cables. The housing has been optimized to enable efficient exchange of

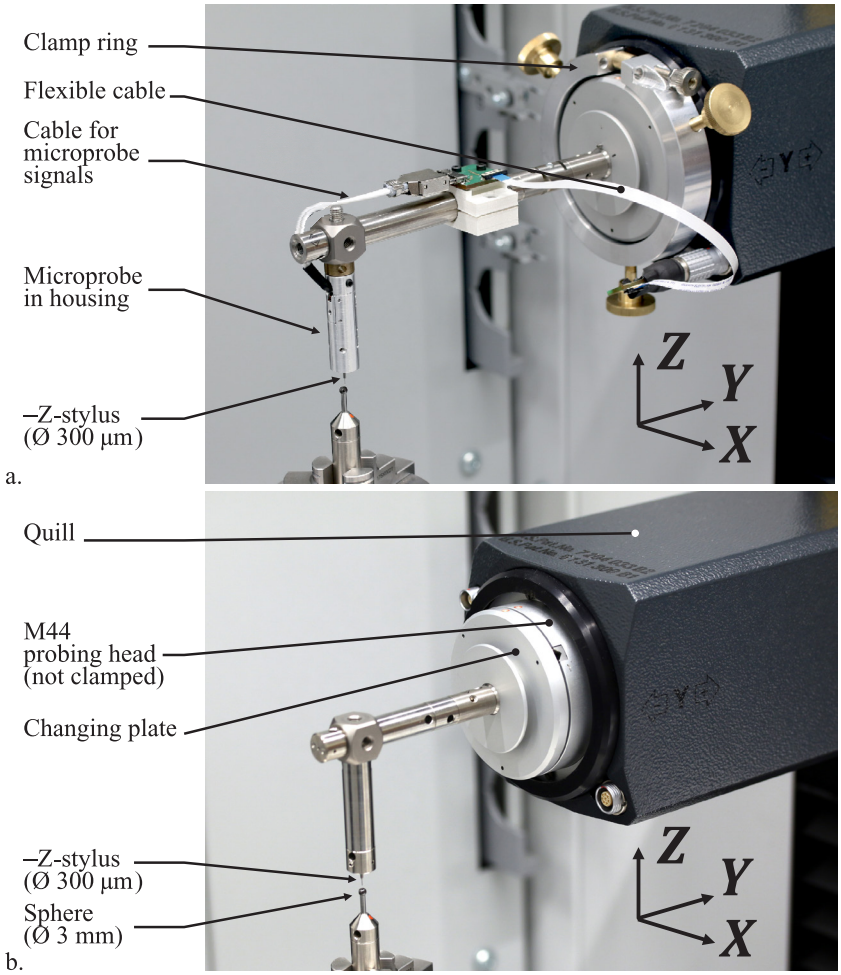


**Figure 8.** (a) Installation of the microprobe on the P40 with the clamped probing head, and (b) detail of the standard setup of the CMM with the probing head M44. Both measuring systems are in a $-Z$-configuration.

microprobes, and to ensure a compact system (external diameter $<$ Ø 11 mm). This housing can be mounted on CMM via the adapter part. A screw can adjust the housing's orientation among its longitudinal axis. As an alternative to gluing a not interchangeable stylus, a micro-changing mechanism has been constructed but was not yet investigated on the microprobe [37]. With the micro-changing mechanism, the holder could be used as a mechanical limit to protect the parallelograms from exceeding a maximum deflection. The changing mechanism could then act as a mechanical fuse to decouple the stylus from the microprobe and to protect the measuring system.

The microprobe in the housing was mounted onto the M44 probing head via a changing plate as a conventional stylus (see figure 8(a)). To investigate the microprobe independently from the M44, a clamp ring was used to mechanically deactivate the M44 and an additional function was implemented from Klingelnberg to consider only the microprobe deflections $m_X, m_Y, m_Z$ during measurements. The three voltages $U_X, U_Y, U_Z$ of the microprobe were transmitted to the CMM through data acquisition modules (Dewetron DAQP-BRIDGE-A), with which the signals were pre-amplified (with a gain of 20) and pre-filtered (100 Hz low pass frequency). After the installation of the microprobe on the machine, the occurring bending offset, especially in the $Z$-direction due to the gravitation, are electronically compensated with the acquisition modules. The modules also provide the 5 V supply voltage for the microprobe. After digitalization through an Analog/Digital-converter module TPMC501 from TEWS Inc., the voltages were converted into deflections $m_X, m_Y, m_Z$ using the matrix $\boldsymbol{C}$ (see equation (1)) in the CMM. To protect the microprobe from collisions, a software limit switch was implemented, which stops any motion when exceeding a maximal deflection. Thanks to the large deflection range and this function, higher measurement and displacement speeds can be used.

The microprobe performances were compared with those of an equivalent standard setup of the CMM (see figure 8(b)) and commercially available probes. In both cases, a stylus made of a ruby probing sphere with a Ø 300 µm diameter and an effective shaft length of 2 mm (Ø 0.2 mm) was employed in a $-Z$-configuration (see figure 8).

### 3.3. Iterative characterization of the microprobe

The conversion matrix $\boldsymbol{C}$ defines the linear relationship between the deflections of the probing element $m_X, m_Y, m_Z$ and the measured voltages $U_X, U_Y, U_Z$ of the microprobe.

**Table 1.** Conversion and verification matrices for each step $i$, $\boldsymbol{C_i}$, $\boldsymbol{C_{i+1}}$ and $\boldsymbol{V_{i+1}}$ for both cube and sphere probing during the characterization.

| $i$ | Probing directions | $\boldsymbol{C_{i-1}}$ in mm · V$^{-1}$ | $\boldsymbol{V_i}$ in $10^{-2}$ | $\boldsymbol{C_i} = \boldsymbol{V_i} \cdot \boldsymbol{C_{i-1}}$ in $10^{-2}$ mm · V$^{-1}$ |
|---|---|---|---|---|
| 1 | Five main axes on a cube | $\begin{bmatrix} 1 & 0 & 0 \\ 0 & 1 & 0 \\ 0 & 0 & 1 \end{bmatrix}$ | $\begin{bmatrix} 6.61 & -0.260 & 0.234 \\ 0.250 & 6.08 & -0.760 \\ 0.0532 & -0.190 & -5.89 \end{bmatrix}$ | $\boldsymbol{C}_1 = \boldsymbol{V}_1$ |
| 2 | 37 directions on a sphere | $\boldsymbol{C}_1$ | $\begin{bmatrix} 0.993 & 0.001 & -0.001 \\ -0.003 & 0.985 & -0.002 \\ 0.004 & 0.002 & 1.010 \end{bmatrix}$ | $\begin{bmatrix} 6.97 & -0.257 & 0.121 \\ 0.263 & 6.20 & 0.0468 \\ 0.111 & -0.158 & 6.08 \end{bmatrix}$ |
| 3 | 37 directions on a sphere | $\boldsymbol{C}_2$ | $\begin{bmatrix} 0.999 & 0.001 & 0.000 \\ 0.000 & 1.000 & -0.001 \\ 0.000 & -0.001 & 0.999 \end{bmatrix}$ | — |

To determine the matrix $\boldsymbol{C}$, a variation of deflections and the corresponding voltage variations were collected during the probing of a cube and a sphere (both with a length and a diameter of 3 mm) (see figure 9), and their relations were computed using a least squares method.

In the beginning, the microprobe behavior and its position in the CMM are entirely unknown. To achieve the first estimation of matrix $\boldsymbol{C}_1$, the microprobe was only probed in its main axis using a cubic artifact to avoid any slipping of the tip, which would have happened with a sphere and the position awareness. During the probing, an arbitrary initial matrix $C_0 = I_3$ (identity matrix) was chosen. The cube was aligned with the main directions within a tolerance of less than 1° with a scanning alignment tool of the machine. Using $\boldsymbol{C}_1$, a provisory referencing of the microprobe could be performed, its position and tip diameter could be determined by probing a Ø 2 mm reference sphere with a calibrated diameter with the standard routine of the machine [33, 46]. Then a sphere was probed and a new matrix $\boldsymbol{C}_2$ could be determined using the new data of the recorded deflections and voltages variations by correcting the matrix $\boldsymbol{C}_1$. During the automatic probing, five points on the cube were probed, corresponding to the main axis of the CMM $\pm X$, $\pm Y$ and $-Z$, and 37 points were uniformly distributed on the top half of the sphere (see figure 9). For each point, the contact with the cube was first detected and the tip was then deflected 10 times (2 times for the sphere) with 5 µm steps (20 µm for the sphere) orthogonally to the probed surface. The microprobe was then characterized over the deflection range of approximately 10 µm–60 µm. For both characterization steps (with cube and sphere) $i = 1$ and $i = 2$ the displacements of the microprobe $D_X, D_y, D_Z$ were calculated from the recorded M44 positions $P_X, P_Y, P_Z$, as $\boldsymbol{D_i} = \Delta \boldsymbol{P_i}$. The recorded deflection of the microprobe $m_X, m_Y, m_Z$ calculated with the used matrix: $\boldsymbol{m_i} = \boldsymbol{C_{i-1}} \cdot \boldsymbol{U_i}$ were compared to $\boldsymbol{D_i}$, with the help of the verification matrix $\boldsymbol{V_i}$ determined by solving the linear least squares problem $\boldsymbol{D_i} = \boldsymbol{V_i} \cdot \boldsymbol{m_i}$ using a QR decomposition [47]. If the matrix $\boldsymbol{C_{i-1}}$ corresponds to the behavior of the microprobe, then $\boldsymbol{D_i}$ is equal to $\boldsymbol{m_i}$ as the displacement corresponds to the deflections (hypotheses of contact with no slipping), and $\boldsymbol{V_i}$ tends to be the identity matrix. In other words, $\boldsymbol{V_i}$ shows how good the matrix $\boldsymbol{C_{i-1}}$ transforms the measured voltages $\boldsymbol{U_i}$ into deflections $\boldsymbol{m_i}$ toward the measured displacements $\boldsymbol{D_i}$ and can be used for correction and building a new matrix $\boldsymbol{C_i} = \boldsymbol{V_i} \cdot \boldsymbol{C_{i-1}}$.

In table 1, the matrices $\boldsymbol{C_i}$ and $\boldsymbol{V_i}$ are given for the microprobe used for the measurement of the artifact presented in section 4.3. The step $i = 3$ is the verification step of the characterization, which is why only the matrix $\boldsymbol{V_i}$ is given. It is observed that the matrices $\boldsymbol{V_i}$ for $i$ from 1 to 3, converge well to the identity matrix. The first matrix enables to have a preliminary conversion matrix, to use the microprobe and to probe the sphere artifact. By probing in a multitude of directions, the matrix and especially the non-diagonal coefficients can be refined. In the case of this microprobe, a crosstalk smaller than 4.2% can be observed between the three axes.

Generally, conventional CMMs—like the one used in this work—lack specific features needed for dimensional micrometrology such as tools for adequate clamping of microworkpieces or vision systems. Furthermore, the environmental conditions of these CMMs (for example, when situated near the production line or on the shop floor) may critically impact the measurement quality. Therefore, to benefit *fully* from the integrated microprobe, a so-called *microenvironment* was designed and realized, which is described in the following.

### 3.4. Microenvironment for dimensional micrometrology

The developed microenvironment strives to overcome some of the challenges of tactile measurements at the microscale regarding handling, cleaning, usability, contamination control, and clamping [48]. The following process chain qualitatively demonstrates the benefits of the system (see figure 10).

The portable microenvironment (see figure 11) consists of *five modules,* which will be detailed in the following paragraphs:

- Passive separative device protecting the direct measurement environment from particles, air-flow, and temperature deviations in harsh environments or on shop floors,
- Clamp for external microgears with a compliant string,
- Dual-camera system featuring manual, 6-DOF articulations to assist during setup and manual positioning of the microprobe addressing the limitations of the human eye,

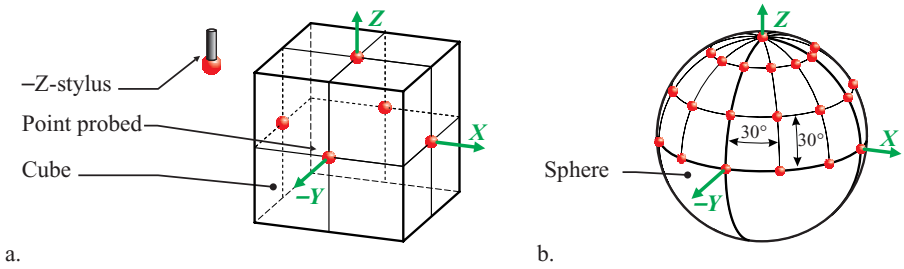


**Figure 9.** Sketch of: (a) the cubic artifact, and (b) the sphere artifact with the probed points for a −*Z*-direction stylus to characterize the microprobe.

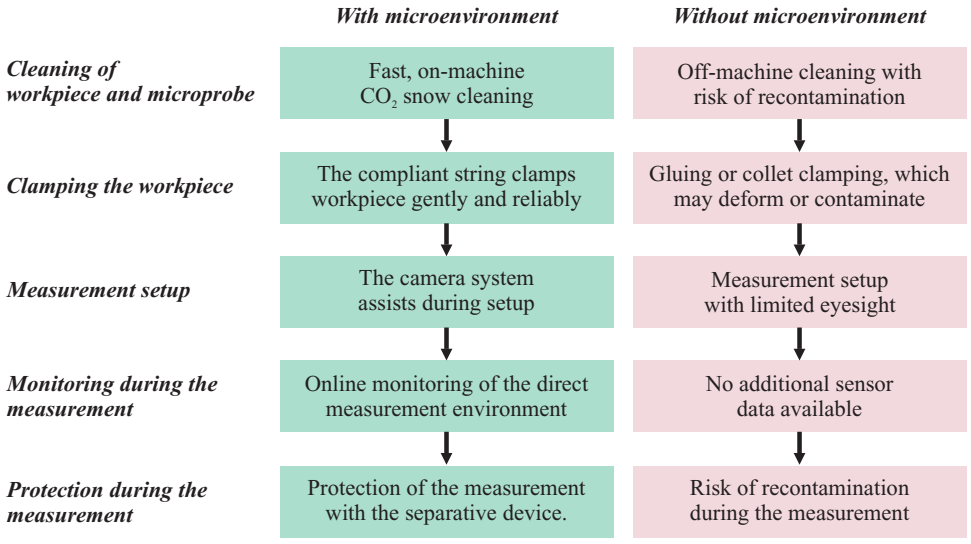


**Figure 10.** Process chain emphasizing the benefit of the microenvironment.

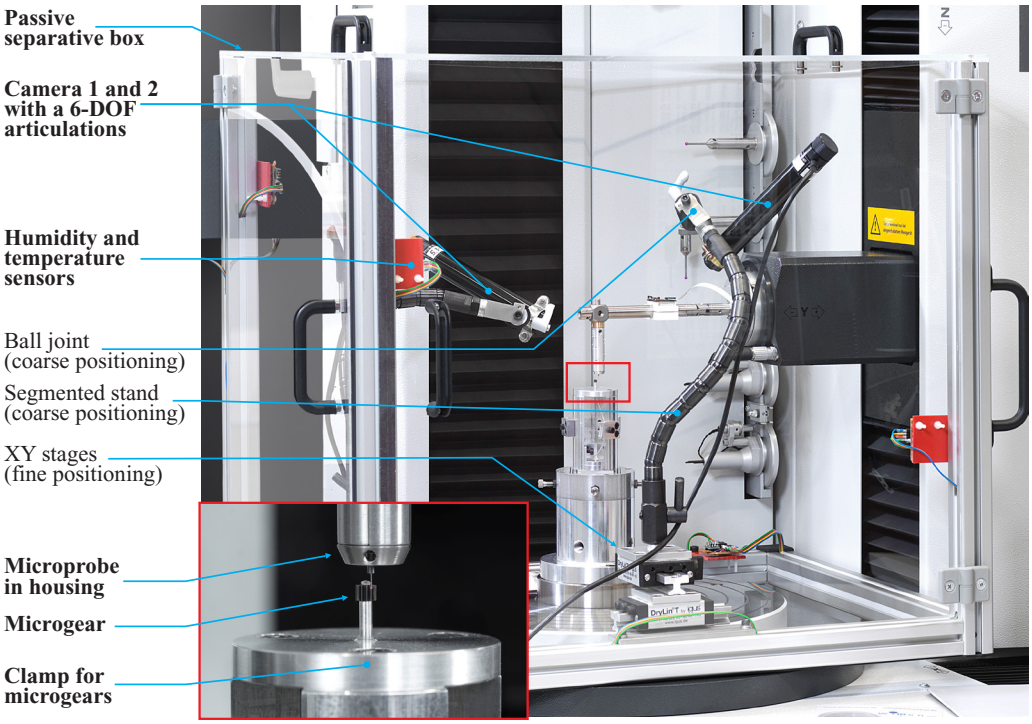


**Figure 11.** The microenvironment developed at PTB and mounted on the Klingelnberg P40.

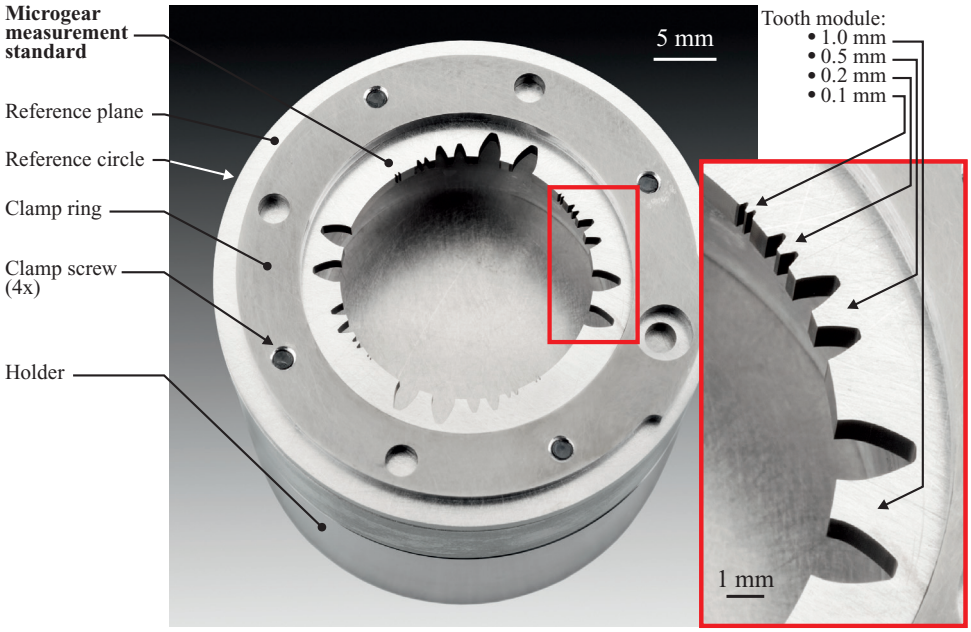


**Figure 12.** Top view of the microgear measurement standard clamped on its holder and detail view of the four teeth modules. The custom clamping minimizes the deformation of the microgear and allows for easy reclamping.

- Online sensor system (four temperature and humidity sensors and a particle sensor),
- $CO_2$ snow cleaning system for *on-machine* cleaning of microprobe and workpiece.

The *separative device* is a cuboid-shaped construction made of aluminum profiles with a size of 56 cm × 50 cm × 46 cm (width × height × depth). The bottom side remains open to allow access to the rotary table. The two sides directed towards the measuring machine also remain open to allow access to the probing system and the automatic stylus changer. Acrylic glass doors seal the remaining three sides (top, front and left side). This design meets the requirements regarding usability, weight, costs, protection against contamination and sudden temperature changes.

In contrast to active microenvironments (see ISO 14644 and [49–51]), this design comes without fans or filters. Reasons for the *passive* approach are lower costs, better portability, and shorter times for stabilization of the setup before measurements. Experiments with particle traps proved that using the separative device decreases the surface contamination on the rotary table of the measuring machine by 32%.

The *compliant-string clamp* reliably clamps microgears with low-cost components [31]. The easy-to-use, fully mechanical process treats the workpieces gently because of the high compliance of the string (made of PA, PVDF, PE or nylon). The clamping force realized by weights is defined and repeatable. Moreover, the clamping principle features an inherent centering mechanism.

The *dual-camera system* allows magnifying the probe tip during setup of the measurement procedure—for instance, for manual probing of the tooth space number one. Using two microscope cameras at an angle of 90° creates a sense of depth, which makes manual 3D-positioning of the microprobe easy and fail-safe, since a collision of the workpiece with the microprobe may break it. The 6-DOF articulation positions the camera to the workpiece for an optimal field of view.

The *sensor system* allows monitoring the environmental parameters inside the separative device, by streaming and logging the data of the five digital sensors for temperature, humidity, and particle density to a local internet address. Thus, real-time information on the quality of the direct environment could be obtained, and measurement errors due to, for instance, high humidity or temperature instabilities may be attributed.

The *$CO_2$ snow cleaning* process using a hand-held cleaning gun is a fast, on-machine cleaning process that removed 25% more particles than high-speed air jet in the experiments [29]. The process is suitable for most workpieces with sub-millimeter features if they resist the thrust pressure—but the same applies for cleaning with a high-speed air jet. The dry ice stream has temperatures down to −78.5 °C but, due to the higher surface-to-volume ratio of micro-objects in comparison to macro objects [52], the time to recover ambient temperature is reasonably short. At high humidity, condensation on the cleaned surfaces can occur, which influences the probing process. However, condensation can usually be avoided by using short cleaning pulses, a tailored cleaning strategy, and by introducing a second gas (e.g. nitrogen purging) that displaces the ambient air [53].

## 4. Verification based on comparison measurements

### *4.1. Overview of the three reference objects*

The three reference objects (cube, sphere, and microgear) feature distinct geometries that help to verify and evaluate the performance of the IMT-PTB microprobe using the amenities of the microenvironment (see table 2).

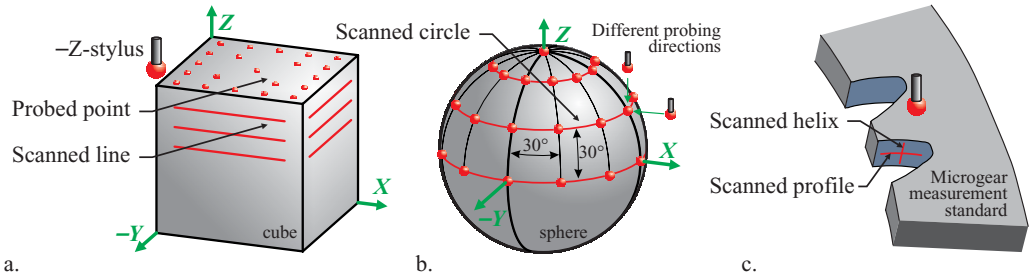


**Figure 13.** Measurements strategies of (a) the cube, (b) the sphere, and (c) the microgear measurement standard.

**Table 2.** Details about the reference objects, which were traceably calibrated by PTB on the Zeiss F25 $\mu$CMM.

| Parameter | Cube | Sphere | Microgear |
|---|---|---|---|
| Size | 3 mm edge length | Ø 3 mm | Ø 20 mm tip diameter |
| Material | Carbide | Silicon nitride | Carbide[a] |
| Calibrated features | Edge length, flatness deviation, straightness, parallelism, angle | Diameter and sphericity | Profile and helix (Slope, form, and total deviations) |
| Tactile probe during calibration | Ø 0.3 mm, Rubin | Ø 0.3 mm, Rubin | Ø 0.3 mm, Rubin |
| Maximum form deviations | 1 µm | 0.14 µm | 5 µm |
| Measurement uncertainties of the calibration | 0.25 µm–0.4 µm, 0.01° | 0.1 µm–0.15 µm | 0.3 µm–0.6 µm |

[a] PTB also manufactured and calibrated a titanium version, which meets the requirements of CT measurements.

The internal microgear measurement standard [54] is workpiece-like and integrates four modules into one workpiece, which improves usability and the range of applications (see figure 12). The gear contours of the measurement standard were manufactured using wire electrical discharge machining.

### 4.2. Overview of the comparison measurements

To verify the integrated microprobe and to compare its performance, the calibrated reference objects were measured using the microprobe and the standard probing setup on the Klingelnberg *P40*. The reference objects were calibrated with the high-precision Zeiss F25 $\mu$CMM for which traceability is proved. Both probing systems measured the same reference objects with the same measurement procedures on the Klingelnberg *P40*, like those for the calibration. The measurements on the P40 were carried out at a controlled temperature of 20 °C ± 0.2 K and the calibration at 20 °C ± 0.1 K, so that thermal effects influencing the results can be neglected. In figure 13, the measurement strategies are shown. On the cube, 26 points along horizontal lines were scanned on three different heights on each side and the top surfaces, 21 points were probed. Out of these, the flatness deviation of each side and width between them could be determined. To determine the diameter and the form deviation of the sphere respective its half calotte, the sphere was probed in two different ways. First, 37 points were probed, where some points were probed by using two different probing directions. In a second way, the sphere was rotated, and a circle on the equator was scanned (360 measurement points). Gaussian elements were employed to fit the sphere and the planes of the cube. After measuring the references plane and circle on the microgear standard, the profile and helix lines of the tooth were scanned with a special gear measurement software tool, which gives the deviation to a nominal profile/helix related to the roll length or facewidth. From these, the typical six gear deviation parameters $f_{H\alpha}$, $f_{f\alpha}$, $F_\alpha$, $f_{H\beta}$, $f_{f\beta}$, and $F_\beta$ can be calculated [54]. The number of repetitions for each measurement (cube, sphere and microgear) was six.

**Table 3.** Measurement results of the cube measurements. The final values used for comparison each are the means of six repetition measurements.

| | Difference to the calibration in µm ($E_n$-scores) | |
|---|---|---|
| | IMT-PTB microprobe | Standard probe |
| Flatness deviation $+Y$ | 0.01 (0.02) | 0.03 (0.05) |
| Flatness deviation $-Y$ | −0.07 (0.1) | −0.18 (0.3) |
| Flatness deviation $+X$ | 0.03 (0.1) | −0.09 (0.2) |
| Flatness deviation $-X$ | −0.10 (0.16) | 0.12 (0.2) |
| Flatness deviation $+Z$ | 0.17 (0.3) | 0.12 (0.2) |
| Edge length $X$ | 0.28 (0.4) | 0.70 (1.1) |
| Edge length $Y$ | 2.34 (3.5) | 2.43 (3.6) |

The differences between these measurement results and calibration values were analyzed. Comparing these results eliminated possible differences between the Klingelnberg *P40* and the Zeiss *F25* used for calibration (for example, software routines). Additionally, $E_n$-scores were calculated as

$$E_n = \frac{|\Delta y|}{\sqrt{U_{\text{cal}}^2 + U_{\text{P40}}^2}} < 1 \rightarrow \text{Successful performance} \qquad (2)$$

for proficiency testing (see ISO 13528) where scores smaller than one indicate a successful performance. The score is calculated by considering the measurement uncertainties of the calibration $U_{\text{cal}}$ and comparison measurement $U_{\text{P40}}$. The $E_n$-score is a proven method for assessing the quality of a

**Table 4.** Measurement uncertainties $U(k = 2)$ in μm for the cube measurements.

| | Measurement uncertainty $U(k = 2)$ in μm | | |
|---|---|---|---|
| | IMT-PTB microprobe | Standard probe | Calibration on Zeiss F25 |
| Flatness deviation | 0.60 | 0.60 | 0.30 |
| Edge length | 0.70 | 0.65 | 0.25 |

**Table 5.** Measurement results of the sphere measurements. The final values used for comparison each are the means of six repetition measurements.

| | Difference to the calibration in μm ($E_n$-scores) | |
|---|---|---|
| | IMT-PTB microprobe | Standard probe |
| Roundness deviation at equator | 0.05 (0.1) | 0.04 (0.1) |
| Diameter | −0.24 (0.4) | −0.45 (0.9) |
| Sphere form deviation | 1.24 (0.9) | 0.44 (0.5) |

measurement result. With $E_n$-scores smaller than one, the measurement values are comparable considering their respective uncertainties.

### 4.3. Measurement results

All measurements were performed using both setups: the one with the integrated microprobe and the standard setup (see figure 8). For both analogue measuring probes, a standard deflection of 50 μm was chosen, but an effective deflection during measurement and reference measurement (e.g. gear) up to 200 μm could be observed, due to the closed-loop scanning, where a fixed path is followed by the CNC control. Before measurements were carried out on the P40, a calibration of the microprobe (and the standard probing system) is needed. During this internal procedure, a *total* stiffness of the stylus is determined experimentally considering the shaft bending but also all phenomena arising from probing deformation (e.g. Hertzian pressure). If the stiffness and hardness of the reference sphere and workpiece comply, the machine software compensates these phenomena. In this section, the measurements results carried out on the three artifacts are presented for both setups and compared to each other using the difference to the calibration values. The measurement uncertainties given for the measurements include the probing system but also the machine axes, the measurement strategy, the environment, etc. The GUM approach was used to determine all measurement uncertainties [55]. The measurement uncertainties given for the *calibration* include the influence of measurement repeatability (single nanometers), temperature drift and offset (single nanometers), form deviation of the probing sphere (nanometers), contamination (single nanometers), and the uncertainty when probing a single measurement point in 3D in a small volume (0.1 μm).

*4.3.1. Cube measurement.* During the experiments, two probes characterized the three calibrated reference objects on the Klingelnberg *P40*. The results are stated as differences to the calibration values (see table 3). The standard deviations of the repetition measurements are similar for both probes and are in the range of 50 nm for sphere and cube. The errors in the edge length measurements can derive from the probing from two sides, which gives rise to errors due to hysteresis, drifts, and the form deviation of the probing sphere. The issue seems not to be related to the IMT-PTB-microprobe because the standard probe exhibits similar errors. Thus, the origin of these errors has not been further investigated yet.

The respective measurement uncertainties needed to compute the $E_n$-scores are given in table 4.

**Table 6.** Measurement uncertainties $U(k = 2)$ in μm for the sphere measurements.

| | Measurement uncertainty $U(k = 2)$ in μm | | |
|---|---|---|---|
| | IMT-PTB microprobe | Standard probe | Calibration on Zeiss F25 |
| Roundness deviation at equator | 0.55 | 0.55 | 0.10 |
| Diameter | 0.50 | 0.45 | 0.15 |
| Sphere form deviation | 1.40 | 0.90 | 0.10 |

*4.3.2. Sphere measurement.* The results of the sphere measurements are stated in table 5. The results of roundness deviation and diameter are satisfying. However, the sphere form measurements show large deviations, which may be due to the measurement strategy: the probing is not perpendicular to the sphere surface but in the direction of the machine axes.

The respective measurement uncertainties needed to compute the $E_n$-scores are given in table 6.

Furthermore, repeatability tests were performed in which the same nominal point on the sphere was probed 16 times. This repeatability test with probing forces normal to the sphere surface was executed for three different points:

- 45° polar angle and 45° azimuthal angle leading to a 3D-deflection (*XYZ*-axes) of the probe
- 90° polar angle (equator) and 45° azimuthal angle leading to a 2D-deflection (*XY*-axes) of the probe
- 90° polar angle (equator) and 0° azimuthal angle leading to a 1D-deflection (*Y*-axis) of the probe

The two evaluated parameters are the mean and the standard deviation of the distances between the 16 points and their center (see table 7). From these tests, a similar behavior of both measuring probes in the P40 can be again observed.

*4.3.3. Gear measurement results and measurement uncertainties.* The quality of the microgear measurements is the central indicator for verification of the IMT-PTB microprobe, because it corresponds to the typical industry use-case. The repeatability for the microgear measurement is larger than for cube and sphere and in the range of 100 nm. The usability of the IMT-PTB microprobe during the comparison measurements was identical to the native probing system. The

**Table 7.** Results of the repeatability tests. According to Klingelnberg, the results improve (numbers are halved) for larger probing sphere and shaft diameter, with which the probe shaft bending is reduced.

| Parameter | Probe deflection directions | IMT-PTB microprobe | Standard probe |
|---|---|---|---|
| Mean distance to the center of the points in µm | 3D | 1.5 | 1.3 |
| | 2D | 1.3 | 0.9 |
| | 1D | 0.1 | 0.3 |
| Standard deviation of the distancesto the center of the points in µm | 3D | 0.9 | 0.8 |
| | 2D | 0.7 | 0.6 |
| | 1D | 0.1 | 0.2 |

**Table 8.** Measurement results stated as differences to the calibration values in µm. The final values used for comparison each are the means of six repetition measurements. The values stated for the microgear are the results from one representative tooth space. The calibration values for the microgear measurement standard are not stated because it would restrict using the standard for comparison measurements where participants should not be aware of the calibration results.

| | Difference to the calibration value in µm ($E_n$-scores) | |
|---|---|---|
| Microgear (1 mm module) | IMT-PTB microprobe | Standard probe |
| Profile slope deviation $f_{H\alpha}$ | −0.43 (0.7) | 0.86 (1.3) |
| Profile form deviation $f_{f\alpha}$ | 0.22 (0.1) | 0.07 (0.1) |
| Total profile deviation $F_\alpha$ | −0.69 (0.6) | 0.55 (0.5) |
| Helix slope deviation $f_{H\beta}$ | −0.39 (0.8) | 0.30 (0.6) |
| Helix form deviation $f_{f\beta}$ | 0.15 (0.6) | −0.68 (0.6) |
| Total helix deviation $F_\beta$ | 0.16 (0.5) | −0.64 (0.6) |

differences to the calibration value are stated in table 8 for the 1 mm module. The measurement results for the 0.5 mm module show similar deviations. To test the proficiency of the IMT-PTB microprobe compared to the standard probe, the $E_n$-scores (see ISO 13528) are given in parentheses for all deviations. The $E_n$-scores were computed using the differences to the calibration values stated in table 8, the measurement uncertainties stated in table 9 and the equation (2). All resulting $E_n$-scores are smaller than one for the IMT-PTB microprobe, which proves the proficiency of the development considering the determined measurement uncertainties. The standard probe yields scores comparable to the IMT-PTB microprobe's performance except for the profile slope deviation where the $E_n$-score is larger than one.

The measurement uncertainties for the gear measurements were computed (see table 9) on the basis of the data obtained earlier during the calibration of the microgear measurement standard [54]. The measurement uncertainties during calibration were smaller due to the higher precision and accuracy of the F25 $\mu$CMM and the more stable measurement environment.

*4.3.4. Discussion.* The results prove the aptitude of the microprobe for coordinate metrology. Especially promising are the results of the microgear measurement where all results lie within the measurement uncertainty of the particular measurands, in contrast to the results using the standard probe.

**Table 9.** Measurement uncertainties $U(k = 2)$ in µm for all six gear deviations.

| | Measurement uncertainty $U(k = 2)$ in µm | | |
|---|---|---|---|
| | IMT-PTB microprobe | Standard probe | Calibration on Zeiss F25 |
| Profile slope deviation $f_{H\alpha}$ | 0.50 | 0.50 | 0.40 |
| Profile form deviation $f_{f\alpha}$ | 0.95 | 1.00 | 0.50 |
| Total profile deviation $F_\alpha$ | 1.00 | 1.00 | 0.60 |
| Helix slope deviation $f_{H\beta}$ | 0.35 | 0.35 | 0.30 |
| Helix form deviation $f_{f\beta}$ | 0.95 | 0.95 | 0.50 |
| Total helix deviation $F_\beta$ | 1.00 | 1.00 | 0.55 |

The robustness of both probes is similar. In the event of a crash with probe deflection of more than 400 µm, both probes fail critically. In the case of the standard probe, the probing shaft usually breaks, but the probing system stays intact. In the case of the IMT-PTB microprobe, the probing system fails and has to be replaced, which comes with higher costs.

The IMT-PTB microprobe's sophisticated level of integration allows for natural use of all software features of the measuring machine. The user will practically not notice a difference.

The main advantages of the IMT-PTB microprobe over the standard probe are the lower probing forces and the smaller probing spheres possible, allowing intrusion into smallest geometries.

## 5. Conclusion and outlook

The developed *isotropic microprobe featuring stacked parallelograms with silicon hinges* was integrated into a standard gear measuring machine to extend its measurement capabilities. The system can measure complex 3D workpieces with high precision featuring probing forces in the range of 15 mN @ 50 µm and maximum deflections in all axes of ±400 µm. The distribution of the IMT-PTB microprobe in cooperation with commercial manufacturers of measuring machines is currently in discussion.

Alongside the development of the microprobe, a *microenvironment* was designed featuring a microgear clamp, a $CO_2$ snow cleaning gun, a dual-camera system, an environmental sensor system, and a separative device. This portable

system facilitates and improves dimensional measurements at the microscale.

Comparison measurements of calibrated reference objects were performed to evaluate and analyze the novel microprobe within the microenvironment. The comparison with the standard Klingelnberg probing system showed that the microprobe is well integrated and capable of performing measurement tasks with the native software and control. The results of the experiments and comparison measurements demonstrate the high potential of the novel microprobe design.

Current and future work focuses on various aspects of the microprobe to optimize it for industrial use. Examples are the *anodic* bonding—instead of the *adhesive* bonding—of the three wafers for the manufacture of the measuring cells. Moreover, automating the assembly of the cells is investigated to improve reliability and reproducibility. Accuracy and precision may be enhanced by resizing the cells and through better evaluation electronics. To improve robustness, an interchangeable stylus system is being investigated, which provides a mechanical fuse, as well as the advance of the stylus exchange for different measurement tasks. Further measurements using the microprobe and styli with Ø 50 µm probing spheres are planned to examine the advantages of the microprobe on the P40 and on other measuring machines (e.g. µCMMs [56]).

In the future, the use of the well-approved ISO 10360-2 and 10360-4 acceptance tests is planned to assess the performance of the microprobe. All experiments described in section 4 assess the performance of the measuring machine and the microprobe as a whole. To check if the P40 is limiting the performances of the microprobe, it will be integrated into other measuring machines, for example, µCMMs with higher precision than the measuring machine used so far.

## Acknowledgments

We gratefully thank our colleagues Michael Neugebauer for calibrating all reference objects and Rudolf Meeß and Christian Wolpert for manufacturing the microgear measurement standard.

We thank Fabian Kleifgen, Peter Erdweg, Sebastian Höschen, and Dieter Bade from Klingelnberg for their support during our research.

The authors acknowledge the financial support from the Deutsche Forschungsgemeinschaft (DFG), under grants 275023116, KN 1181/1-1 and DI 1934/5-1.

We gratefully acknowledge the support of the Braunschweig International Graduate School of Metrology (B-IGSM).

## Conflict of interest declaration

Hereby the authors declare no undisclosed funding source and no relationship that may pose a conflict of interest.

## ORCID iDs

D Metz https://orcid.org/0000-0001-6498-8909
S Jantzen https://orcid.org/0000-0001-5810-9779
A Dietzel https://orcid.org/0000-0003-2090-6259

## References

[1] Weckenmann A, Estler T, Peggs G and McMurtry D 2004 Probing systems in dimensional metrology *CIRP Ann.–Manuf. Technol.* **53** 657–84
[2] Weckenmann A, Peggs G N and Hoffmann J 2006 Probing systems for dimensional micro- and nano-metrology *Meas. Sci. Technol.* **17** 504–9
[3] Thalmann R, Meli F and Küng A 2016 State of the art of tactile micro coordinate metrology *Appl. Sci.* **6** 150
[4] Lewis A J 2003 Fully traceable miniature CMM with submicrometer uncertainty *Proc. SPIE* **5190** 265–76
[5] Werth Messtechnik GmbH 2018 *Fiber Probe WFP 3D—High Precision 3D Measurement* https://www.werth.de/en (Accessed: 9 September 2018)
[6] MITUTOYO 2018 *UMAP Vision System* http://www.mitutoyo.co.jp/eng/ (Accessed: 12 September 2018)
[7] Zeiss 2019 *Datasheet F25* https://www.centerfreeformoptics.org/wp-content/uploads/2014/08/f25_brochure.pdf (Accessed: 16 July 2019)
[8] Bos E, Moers T and van Riel M 2015 Design and verification of an ultra-precision 3D-coordinate measuring machine with parallel drives *Meas. Sci. Technol.* **26** 85904
[9] Xpress Precision Engineering B.V. 2019 *Ultra Precision Metrology Solutions* https://www.xpresspe.com/index.php (Accessed: 5 December 2018)
[10] Linz S, Schoch A, Bach C, Ettemeyer A, Hopp B and Andras M 2012 3D fiber probe: State of the art and new developments *International Symposium on Optomechatronic Technologies (ISOT), 2012: 29–31 Oct. 2012, Paris, France 2012 International Symposium on Optomechatronic Technologies (ISOT 2012) (Paris, France) (Paris, France, 29–31 October 2012)* ed Y Bellouard (Piscataway, NJ: IEEE) pp 1–4
[11] Muralikrishnan B, Stone J A and Stoup J R 2006 Fiber deflection probe for small hole metrology *Precis. Eng.* **30** 154–64
[12] Peggs G N, Lewis A J and Oldfield S 1999 Design for a compact high-accuracy CMM *CIRP Ann.–Manuf. Technol.* **48** 417–20
[13] Küng A, Meli F and Thalmann R 2007 Ultraprecision micro-CMM using a low force 3D touch probe *Meas. Sci. Technol.* **18** 319–27
[14] Ferreira N, Brennecke A, Dietzel A, Buttgenbach S, Krah T, Metz D, Kniel K and Hartig F 2013 Reducing the probe ball diameters of 3D silicon-based microprobes for dimensional metrology *2013 Seventh International Conference on Sensing Technology (ICST) 2013 Seventh International Conference on Sensing Technology (ICST) (Wellington, New Zealand, 3/12/2013–5/12/2013)* (IEEE) pp 301–6
[15] Tibrewala A, Phataralaoha A and Büttgenbach S 2008 Analysis of full and cross-shaped boss membranes with piezoresistors in transversal strain configuration *J. Micromech. Microeng.* **18** 55001
[16] Bütefisch S, Büttgenbach S, Kleine-Besten T and Brand U 2001 Micromechanical three-axial tactile force sensor for micromaterial characterisation *Microsyst. Technol.* **7** 171–4
[17] Bos E J C *Tactile 3D probing system for measuring MEMS with nanometer uncertainty: Aspects of probing, design, manufacturing and assembly* (Technische Universiteit Eindhoven
[18] Goj B, Dressler L and Hoffmann M 2015 Design and characterization of a resonant triaxial microprobe *J. Micromech. Microeng.* **25** 125011

[19] Claverley J D and Leach R K 2013 Development of a three-dimensional vibrating tactile probe for miniature CMMs *Precis. Eng.* **37** 491–9

[20] Cho C-H 2009 Characterization of Young's modulus of silicon versus temperature using a 'beam deflection' method with a four-point bending fixture *Curr. Appl. Phys.* **9** 538–45

[21] Shirai K 2013 Temperature dependence of Young's modulus of silicon *Japan. J. Appl. Phys.* **52** 88002

[22] Vanhellemont J, Swarnakar A K and van der Biest O 2014 Temperature Dependent Young's Modulus of Si and Ge *ECS Trans.* **64** 283–92

[23] Muhlstein C L, Brown S B and Ritchie R O 2001 High-cycle fatigue of single-crystal silicon thin films *J. Microelectromech. Syst.* **10** 593–600

[24] Barlian A A, Park W-T, Mallon J R, Rastegar A J and Pruitt B L 2009 Review: semiconductor piezoresistance for microsystems *Proc. IEEE Inst. Electr. Electron. Eng.* **97** 513–52

[25] Smith C S 1954 Piezoresistance effect in germanium and silicon *Phys. Rev.* **94** 42–9

[26] Buetefisch S, Dai G, Danzebrink H-U, Koenders L, Solzbacher F and Orthner M P 2010 Novel design for an ultra high precision 3D micro probe for CMM applications *Proc. Eng.* **5** 705–12

[27] Bos E J C, Heldens R W P, Delbressine F L M, Schellekens P H J and Dietzel A 2007 Compensation of the anisotropic behavior of single crystalline silicon in a 3D tactile sensor *Sens. Actuators* A **134** 374–81

[28] Metz D, Ferreira N and Dietzel A 2017 3D piezoresistive silicon microprobes with stacked suspensions for tailored mechanical anisotropies *Sens. Actuators* A **267** 164–76

[29] Jantzen S, Stein M, Kniel K and Dietzel A 2017 Microclamping principles from the perspective of micrometrology—a review *Precis. Eng.* **50** 538–50

[30] Kinnell P K and Habeb R R 2013 An evaluation of cleaning methods for micro-CMM probes *Meas. Sci. Technol.* **24** 85603

[31] Jantzen S, Meeß R, Stein M, Kniel K and Dietzel A 2017 Clamping of microgears with a compliant string *MacroScale 2017: Recent developments in Traceable Dimensional Measurements (Espoo, Finnland, 17–19 October)* (https://doi.org/10.7795/810.20180323B)

[32] Jantzen S, Decarreaux T, Stein M, Kniel K and Dietzel A 2018 $CO_2$ snow cleaning of miniaturized parts *Precis. Eng.* **52** 122–9

[33] Ferreira N, Krah T, Jeong D C, Metz D, Kniel K, Dietzel A, Büttgenbach S and Härtig F 2014 Integration of a silicon-based microprobe into a gear measuring instrument for accurate measurement of micro gears *Meas. Sci. Technol.* **25** 64016

[34] Ferreira N, Metz D, Dietzel A, Buttgenbach S, Krah T, Kniel K and Hartig F 2013 3D micro probing systems for gear measurements with nanometer-scale deviation *2013 International Conference on Manipulation, Manufacturing and Measurement on the Nanoscale (3M-NANO)* pp 253–8

[35] Metz D, Ferreira N, Chaillot J, Stein M, Kniel K and Dietzel A 2019 Integration of a piezoresistive microprobe into a commercial gear measuring instrument *Precision Engineering* **55** 349–60

[36] Metz D and Dietzel A 2017 New parallelogram 3D-displacement sensor for micro probing and dimensional metrology *Transducers'17, Kaohsiung 19th International Conference on Solid-State Sensors, Actuators and Microsystems (TRANSDUCERS) (Kaohsiung)* (Piscataway, NJ: IEEE) pp 982–5

[37] Metz D and Dietzel A 2018 3-D Isotropic Tactile Microprobe Based on a Silicon Parallelogram Kinematic: From Concept to Fabrication *J. Microelectromech. Syst.* 1–14

[38] Metz D and Dietzel A 2017 Mikrotaster und verfahren zur herstellung *DE* 102017206145 B3

[39] Garcés-Schröder M, Metz D, Hecht L, Iyer R, Leester-Schädel M, Böl M and Dietzel A 2018 Characterization of skeletal muscle passive mechanical properties by novel micro-force sensor and tissue micro-dissection by femtosecond laser ablation *Microelectron. Eng.* **192** 70–6

[40] Garcés-Schröder M, Metz D, Leester-Schädel M and Dietzel A 2015 Micromechanical systems for the mechanical characterization of muscle tissue *Proc. Eng. ineering* **120** 849–52

[41] HBM 2018 *How Does a Bending Beam Load Cell Work?|Working Principle* https://www.hbm.com/en/2973/how-does-a-bending-beam-load-cell-work/ (Accessed: 9 September 2018)

[42] Futek 2018 *LSM250 Parallelogram Load Cell* http://www.futek.com/product.aspx?stock=FSH03923 (Accessed: 9 September 2018)

[43] VPG Transducers–Vishay Precision Group *Load Cell Technology—Technical Note* https://vpgtransducers.com/pca/name/1142 (Accessed: 9 September 2018)

[44] Richter C, Krah T and Büttgenbach S 2012 Novel 3D manufacturing method combining microelectrial discharge machining and electrochemical polishing *Microsyst. Technol.* **18** 1109–18

[45] Klingelnberg GmbH 2018 *P40—KLINGELNBERG Precision Measuring Center* https://www.klingelnberg.com/ (Accessed: 16 August 2018)

[46] Metz D, Ferreira N, Chaillot J, Stein M, Kniel K and Dietzel A 2019 Integration of a piezoresistive microprobe into a commercial gear measuring instrument *Precis. Eng.* **55** 349–60

[47] Venkateshan S P and Swaminathan P (ed)2014 *Computational Methods in Engineering* (Kidlington: Academic)

[48] Stephan Jantzen 2019 *Design of a high-precision microgear metrology system* (Bremen: Carl Ed. Schünemann KG)

[49] Hu S C, Chuah Y K and Yen M C 2002 Design and evaluation of a minienvironment for semiconductor manufacture processes *Build. Environ.* **37** 201–8

[50] Fassi I 2017 *Micro-Manufacturing Technologies and Their Applications: A Theoretical and Practical Guide (Springer Tracts in Mechanical Engineering)* (Cham: Springer International Publishing)

[51] Fan K C, Wang H M and Liu Y C 2008 Development of a constant temperature environment chamber with high stability *MSF* **594** 78–83

[52] Wautelet M 2001 Scaling laws in the macro-, micro- and nanoworlds *European J. Phys.* **22** 601–11

[53] Sherman R 2019 Carbon Dioxide Snow Cleaning Applications *Developments in surface contamination and cleaning: Volume 11: Applications of cleaning techniques* ed K L Mittal and R Kohli (Amsterdam: Elsevier) pp 97–115

[54] Jantzen S, Neugebauer M, Meeß R, Wolpert C, Dietzel A, Stein M and Kniel K 2018 Novel measurement standard for internal involute microgears with modules down to 0.1 mm *Meas. Sci. Technol.* **29** 125012

[55] Joint Committee for Guides in Metrology 2019 *Evaluation of measurement data—Guide to the expression of uncertainty in measurement* https://www.bipm.org/en/publications/guides/gum.html (Accessed: 17 June 2019)

[56] Yu L, Molnar G, Bütefisch S, Werner C, Meeß R, Danzebrink H-U and Flügge J 2018 Micro Coordinate Measurement Machine (uCMM) using voice coil actuator with interferometric position feedback *Tenth International Symposium on Precision Engineering Measurements and Instrumentation 10th International Symposium on Precision Engineering Measurements and Instrumentation (ISPEMI 2018) (Kunming, China, 08.08.2018–10.08.2018)* ed J Tan and J Lin (SPIE) (https://doi.org/10.1117/12.2511527)